Article

Analogous Black Holes in Type-III Dirac Semimetal $Ni_3In_2X_2$ (X = S, Se)

Christopher Sims (iD)

Elmore Family School of Electrical and Computer Engineering, Purdue University, West Lafayette, IN 47907, USA; sims58@purdue.edu

Abstract: Black holes are objects that have a large mass and curve space time, characterized by their event horizon and singularity. Recently, an interesting concept of analogous black holes has emerged in the field of condensed matter physics. In this work, the possibility of realizing analogous black holes in topological material is $Ni_3In_2X_2$ (X = S, Se) discussed. This work shows that the type-III Dirac cones of the material can lead to the emergence of an event horizon and the formation of a black hole-like region near the Dirac point. In addition, the possible experimental signatures of such a system are discussed and the potential implications of an analogous black hole for the study of black hole physics in condensed matter systems.

Keywords: black hole; Dirac; topological

1. Introduction

Black holes are extreme objects in the universe, characterized by their large gravitational pull, event horizon, and singularity [1,2]. Black holes have been the subject of intense study in physics and astrophysics due to their unique properties and their potential implications in understanding the nature of gravity and the universe as a whole.

Recently, the concept of analogous black holes has emerged in the field of condensed matter physics [3,4]. Analogous black holes are not actual black holes but systems that mimic some of the properties of black holes, such as an event horizon and a Hawking-like radiation [5,6]. The emergence of analogous black holes in condensed matter systems has been a subject of intense research in recent years, with several proposals and experimental realizations. The study of photon interactions has been seen to have analogous effect to a black hole horizon [7,8]. More recently, topological systems have been proposed to have ideal states for the study of analogous gravitational interactions in black holes [9–17], or for analogous wormholes [18–20].

Topological materials are a class of materials characterized by their nontrivial band topology, which gives rise to a range of exotic electronic properties [21,22]. Weyl semimetals are materials where the valence and conduction band touch at single points in the band structure. Due to mirror symmetry, the touching points become split in momentum about the mirror plane with opposite chirality. These points of opposite chirality then become connected by Fermi arcs [23–27]. Dirac semimetals are materials which form when a band gap opens in a material due to strong spin orbit coupling interactions and the material is also protected by time-reversal symmetry from the formation of a surface state [28–30] semi-metals. Dirac cones can also have 3D bulk dispersions from symmetry protected states in a bulk band gap [31,32]. In addition, Dirac cones can become strongly tilted, breaking Lorentz invariance [33,34]. Another type of topological material is one with band touching points which are protected by inversion symmetry which forms nodal line semi-metals [35–39]. It is shown that topological properties of the material can lead to the emergence of an event horizon and the formation of a black hole-like region in the system within the SYK model [40]. Experimental signatures of such a system can be used to explore analogous black hole physics within the field of condensed matter physics.

Recently, a new type of Dirac semimetal phase, called type-III, has been predicted to exist in some materials [41,42]. In type-III Dirac semimetals, the Dirac cones are tilted, leading to an anisotropic dispersion relation. This results in an unusual electronic structure that exhibits a number of exotic properties, such as chiral anomaly and topological Lifshitz transitions [43,44].

In this paper, topological materials $Ni_3In_2S_2$ and $Ni_3In_2Se_2$ are studied, which have recently been found to exhibit an endless nodal-line phase near the Fermi level [45]. Using first-principles calculations, The electronic structure of $Ni_3In_2S_2$ and $Ni_3In_2S_2$ are investigated and presence of a type-III Dirac semimetal phase is found in the band structure. Experimental measurements are proposed in order to study analogous black hole physics effects in the strongly gapped type-III Dirac semimetal $Ni_3In_2Se_2$.

2. Materials and Methods

Band structure calculations were performed with the density functional theory (DFT) program Quantum Espresso (QE) [46], accelerated with GPU support on CUDA version 11.7. The exchange correlation functional employed was the generalized gradient approximation (GGA) [47]. Projector augmented wave (PAW) pseudo-potentials were generated using PSlibrary [48]. Crystal structures were obtained from the materials project and generated for input into quantum espresso [49,50] for $Ni_3In_2S_2$ and $Ni_3In_2Se_2$. The relaxed crystal parameters were used to calculate the band structures Table S1. The energy cutoff was set to 100 Ry and charge density cutoff was set to 400 Ry for the plane wave basis. A k-mesh of $25 \times 25 \times 25$ was used for NSCF and wannierization. The high symmetry point K-path parameters were selected SSSP-SEEK path generator [51,52]. The bulk band structure Figure 1 was calculated from the SCF calculation in Quantum Espresso. Topological number analysis was conducted using the Wilson loop algorithm provided by the WannierTools package.
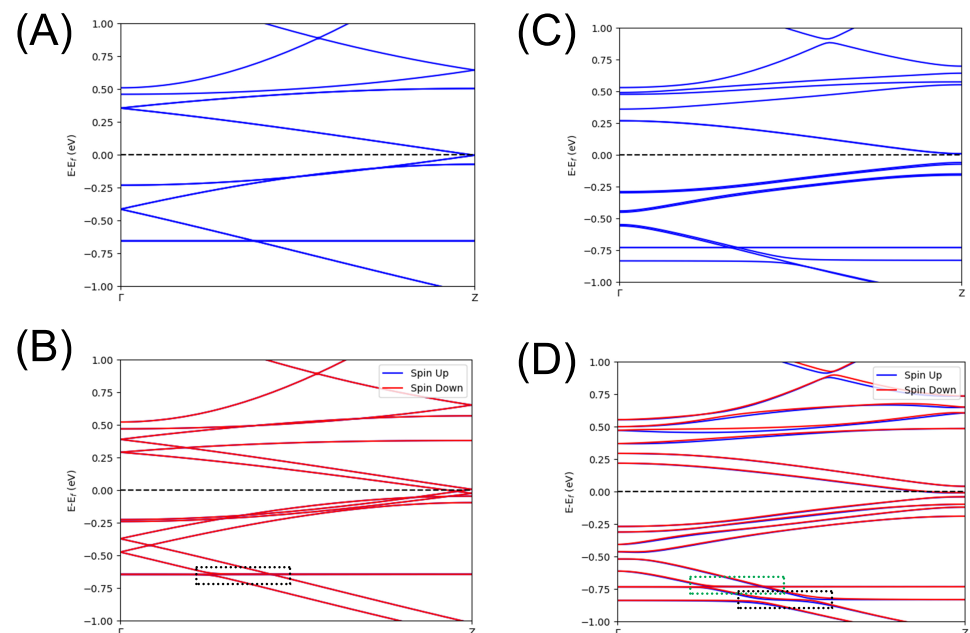

Figure 1. Bulk Band structure: The bulk band structure of $Ni_3In_2S_2$ along the Γ-Z high symmetry line; (**A**) Without spin–orbit coupling, (**B**) with spin–orbit coupling. $Ni_3In_2Se_2$; (**C**) Without spin–orbit coupling, (**D**) with spin–orbit coupling.

$Ni_3In_2S_2$ and $Ni_3In_2S_2$ single crystals (SG: R$\bar{3}$M [166]) were grown using the Indium flux method [53,54]. Stoichiometric quantities of Ni (99.9%, Alfa Aesar) and Se (~200 mesh, 99.9%, Alfa Aesar)/S (~325, 99.5%, Alfa Aesar) were ground together with a mortar and

pestle. To facilitate flux growth, a significant excess of Indium (99.99%, RotoMetals) was added to the mix ($\geq$50%). Subsequently, all precursor materials were carefully sealed within a vacuum-sealed quartz tube and positioned inside a high-temperature furnace. The temperature was gradually raised to 1000 °C over a duration of 1440 min and maintained at that level for an additional 1440 min. Subsequently, a controlled cooling process gradually decreases the temperature to 950 °C within 180 min, followed by a 2880-min dwell period at 950 °C. Finally, the sample was slowly cooled down to 180 °C before being removed from the furnace and placed centrifuge. The grown crystals were characterized using LEED (OCI LEED 600) and powder X-ray diffraction (XRD) (Bruker D8 DISCOVER, Cobalt Source) in order to validate their crystal structure. The XRD results and calculations in order to compare specific features within the calculated XRD pattern [Figure S2].

3. Results and Discussion

3.1. SYK Model

The Sachdev-Ye-Kitaev (SYK) model is a quantum many-body system that is exactly solvable. the SYK is able to accurately model 2D gravity, which is ideal for an accurately solvable model for black holes. Where ψ_i are Majorana fermions, and $J_{i_1 i_2 i_3 \cdots i_n}$ are random couplings with a Gaussian distribution. The parameter O is used to capture higher order terms [55–57].

$$H = \sum_{i_1 < i_2 < i_3 \cdots < i_n} J_{i_1 i_2 i_3 \cdots i_n} \psi_{i_1} \psi_{i_2} \psi_{i_3} \cdots \psi_{i_n} - \frac{\mu}{n!} \sum_{i_1 < i_2 < i_3 \cdots < i_n} \psi_{i_1} \psi_{i_2} \psi_{i_3} \cdots \psi_{i_n} + O \quad (1)$$

In the SYK model, the μ parameter is called the "mass" term. In the context of black holes, the parameter μ is related to the temperature and entropy of the black hole, and plays an important role in the calculation of thermodynamic properties using the SYK model.

Contrarily, for normal interacting Dirac Fermions in 2D, the SYK model takes the form [58]:

$$H = \sum_{i_1 < i_2 < i_3 \cdots < i_n} J_{i_1 i_2 i_3 \cdots i_n} \psi_{i_1}^\dagger \psi_{i_2} \psi_{i_3}^\dagger \cdots \psi_{i_n} - \frac{\mu}{n!} \sum_{i_1 < i_2 < i_3 \cdots < i_n} \psi_{i_1}^\dagger \psi_{i_2} \psi_{i_3}^\dagger \cdots \psi_{i_n} + O \quad (2)$$

where ψ_x are Dirac Fermions, $J_{i_1 i_2 \dots i_q}$ are random couplings with a Gaussian distribution q is the order of the interaction. For the critically tilted regime, a term for the dispersion of the Dirac Fermions is added [59–61].

$$H = \sum_{i_1 < i_2 < i_3 \cdots < i_n} J_{i_1 i_2 i_3 \cdots i_n} c_{i_1}^\dagger c_{i_2} c_{i_3}^\dagger \cdots c_{i_n} + \sum_{<i,j>} t_{ij} c_i^\dagger c_j - \frac{\mu}{n!} \sum_{i_1 < i_2 < i_3 \cdots < i_n} c_{i_1}^\dagger c_{i_2} c_{i_3}^\dagger \cdots c_{i_n} + O \quad (3)$$

c_i are the operators for Fermions, $J_{i_1 i_2 i_3 \cdots i_n}$ are random couplings with a Gaussian distribution, t_{ij} is a hopping parameter that describes the band structure of the Dirac cone and μ is the chemical potential. Since all of these models are exactly solvable, it is possible to measure the dispersion and interaction of Fermions (or Majorana Fermions) in these models.

In the critically tilted Dirac cone (Type-III), the Dirac point lies at the same energy as one of the cone's edge states. The bands in the Dirac cone follow the relation $\psi_i^\dagger(\mathrm{k}) = \psi_j(-\mathrm{k})$. However, at the energy of the Dirac points, the degeneracy forces the flat edge state to have the relation $\psi_i^\dagger = \psi_j$, for all states in the flat band, this creates the ideal analogue for the SYK model at the Dirac point energy and is not realized in type-III Weyl semimetals nor type-II and type-I Dirac cones. In this regime, Dirac Fermions behave like Majorana Fermions [61]. Therefore, pseudo black hole interactions can be probed in condensed matter systems.

3.2. Low Energy Model

In order to visualize the tilted nature of Dirac cones, a simple two band model is constructed which simulates $\sum_{<i,j>} t_{ij} c_i^\dagger c_j$, the Hamiltonian consists of both off diagonal

and diagonal elements, as oppose to the normal Dirac Hamiltonian, which only has off diagonal elements. The diagonal term are used to tune the Dirac cone to different angles.

$$H(k) = \begin{bmatrix} v_f k_x + v_f k_y & v_x k_x - i v_y k_x \\ v_x k_x + i v_y k_x & v_f k_x + v_f k_y \end{bmatrix} \tag{4}$$

Solving the Hamiltonian yields the Eigenvalues for the upper and lower bands. The SYK parameters to the total Hamiltonian are negligible in the two band model, since it only contributes an integer to the eigenvalues [62].

$$E_{\pm}(k) = (v_f k_x + v_f k_y) \pm \sqrt{(v_x k_x)^2 + (v_y k_y)^2} \tag{5}$$

The tilt of the Dirac cone can be determined by the tuning parameter $\eta = \sqrt{(v_f/v_x)^2 + (v_f/v_y)^2}$. ($\eta < 1$) corresponds to the type-I Dirac cone, ($\eta > 1$) is the type-II phase, and ($\eta = 1$) is the type-III phase. Colormaps are for visual aid and do not represent the density of states

The Dirac cone can have three main phases, its type-I normal phase [Figure 2A], its critically tilted type-III phase [Figure 2C], and its over tilted phase [Figure 2B]. By changing the interaction terms in the SYK model, it is possible to model all of these Dirac cone phases within the toy model with *n* interaction terms and only 2D hoping parameters. Within this work, only the type-III phase is of interest.
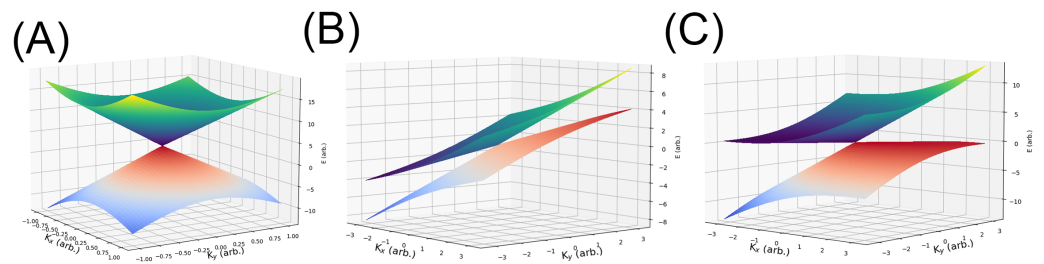
(A)   (B)   (C)

Figure 2. Tilted Dirac Cone: An illustration of the tilted Dirac cone in its (**A**) type-I normal phase (**B**) over-tilted type-II Phase, and (**C**) critically tilted type-III phase.

3.3. Bulk Band Structure of $Ni_3In_2X_2(X = S, Se)$

Single crystals of $Ni_3In_2X_2(X = S, Se)$ and analyzed with powder XRD and are found to have good agreement with their predicted crystal structure [Figure S2 Supplementary Materials]. The calculated crystal parameters are a = b = 5.432 , c = 13.606 for $Ni_3In_2Se_2$ and a = b = 5.432 , c = 13.482104 for $Ni_3In_2S_2$. The single crystal nature of $Ni_3In_2X_2(X = S, Se)$ is also analysis with LEED measurements and are found to have perfect hexagonal shape associated with the R$\bar{3}$M space group.

Bulk band calculations show that there is a flat band in the Γ-Z direction about −700 meV below the Fermi level for $Ni_3In_2S_2$ [Figure 1A], and two flat bands −750 meV and −800 meV Below the Fermi level for $Ni_3In_2Se_2$ [Figure 1C]. Detailed analysis shows that these bands are perfectly flat to within 4 digits ±0.00005 eV (±0.05 meV) for the entire high symmetry line (where 0.0001 is the limit of the accuracy). However, the region of interest are the type-III Dirac cones that form in the gap when spin orbit coupling is applied. $Ni_3In_2S_2$ opens two type-III Dirac cones with a gap ∼10 meV which are iso-energy and are connected by the flat bulk band [Figure 1B, dashed box]. $Ni_3In_2S_2$ opens two sets of type-III Dirac cones with a gap of ∼10 meV for the upper two cones [Figure 1D, green dashed box], and a gap of ∼30 meV for the lower two Dirac cones [Figure 1D, black dashed box]. It is important to note that there is also a momentum (*K*) gap for the Dirac cones in the type-III case. In order to confirm the topological nature of the Dirac cones, $\mathbb{Z}_2$ analysis is conducted and it is found that there is nontrivial topology near the predicted spots for the Dirac cones. The topological number analysis shows that there are prominent areas

which have a strong topological charge and only occur at certain planes when performing $\mathbb{Z}_2$ loop analysis, leading to peaks in the loop analysis when typically smooth curves are expected. (see supplementary for topological charge analysis).

4. Strong Anisotropic Optical Response

Magneto-transport probes of type-III Dirac semi-metals has already been discussed in detail [43], therefore, another method of measuring an analogous black hole is provided.

Optical response can be seen as a good indicator of the electrical properties of a material, especially under the high frequency regime where light operates. In order to calculate the total conductivity of a metal the Kubo-Greenword formula can be utilized, since the transverse conductivity vanishes, only the diagonal terms of the equation remain. The total conductivity σ_{ii} composes from two components σ_{ii}^{intra} and σ_{ii}^{inter} [63,64].

$$\sigma_{ii}^{intra} = \frac{ge^2 v_i}{6\pi^2 \hbar^3 v_j v_k} \frac{\tau}{i\omega\tau - 1} \int_{-\infty}^{\infty} \frac{\partial f_D(\epsilon)}{\partial \epsilon} \epsilon^2 d\epsilon \tag{6}$$

where g is the degeneracy v_i is the respective Fermi velocity, τ is the inelastic scattering time, ω is the frequency of the incident light, and $f_D(\epsilon)$ is the Fermi–Dirac distribution.

$$\sigma_{ii}^{inter} = \frac{ige^2 v_i \omega}{3\pi^2 \hbar^2 v_j v_k} \left[i \int_0^{\epsilon_c} \frac{G_D(\epsilon) - G_D(\hbar\omega/2)}{\hbar^2 \omega^2 - 4\epsilon^2} \epsilon d\epsilon \right] \tag{7}$$

where $G_D(\epsilon) = f_D(-\epsilon) - f_D(\epsilon)$. By taking advantage of the fact that both of these equations calculate the anisotropy of the same bands, the ratio can be simplified to $\sigma_{yy}(\omega)/\sigma_{xx}(\omega) = m_x/m_y$. Thusly, the optical response can be calculated as:

$$\sigma(\theta, v, \omega) = \sigma_{xx} \cos^2(\theta) \sin^2(v) + \sigma_{yy} \sin^2(\theta) \sin^2(v) + \sigma_{zz} \cos^2(v) \tag{8}$$

in which σ shows a dependence on polarization angles v and θ.

In order to measure the optical response of a material, there are two main candidates, optical transmission in which an incident light is shone through a thin film of materials and the transmitted light is measured, or to measure with spectral ellipsometry. Spectral ellipsometry is a better choice since it is better able to measure materials which are single crystals or have little bulk transmittance. Ellipsometry is a technique in which light is sent at an incidence to a surface of a clean material and the reflectance is measured with a detector. In this experimental setup, both the angle of the source light and the polarization can be changed. If needed, the frequency of light can also be changed. With this technique, it is possible to measure single crystals of p-doped $Ni_3In_2As_xSe_{2-x}$, tuned so that it is near the level of the type-III Dirac cone. The normal expected response of a metal is for there to be an anisotropy with respect to the incidence angle θ [Figure 3A], but for there to be no change in the optical response with the polarization angle v [Figure 3B]. For the type-III Dirac cone, there will be a strongly anisotropic response in both the incidence angle [Figure 3C], and the polarization angle [Figure 3D].

Super-radiant (SR) scattering for black holes can be described by the Teukolsky Equation [65]. The Teukolsky equation is not an exactly solvable model and must be solved via numerical methods. However, proposals have shown that SR scattering is an ideal test for general relativity near a black hole (where it breaks down) [66]. Dirac Fermions have been theoretically shown to also be an ideal test of SR scattering near a black hole in Kerr spacetime [67] where Kerr spacetime provides an ideal test bed for testing particle physics on a black hole [68,69]. It has been proposed, that an anisotropic response in the optical conductivity which is proportional to the polarization of light is equivalent to super radiance which is predicted to exist around black holes [70]. It can be seen that there is an over/under reflection of light which varies with polarization angle [Figure 3C,D]. Upon varying the frequency of light, there is expected to be a region (which corresponds to the band gap energy) where the reflectance is far greater than other regions in the frequency

range [70]. for the experiment alight is sent at an incidence angle of 45° to a single crystal of p-doped $Ni_3In_2As_xSe_{2-x}$ (with respect to the Ĉ-axis). In order to probe only the "black-hole" side of the type-III Dirac cone, the laser should be circularly polarized by sending a laser that is linearly polarized through a quarter wave plate and an angle of 45°. In order to detect the reflected light, and analyzer (polarizer) with a photodetector can be setup on the reflected side. When varying the wavelength of light, a strong increase in reflectance at a certain wavelength will correspond to superradiance. Strong optical anisotropy is also a strong indicator of superradiance in $Ni_3In_2Se_2$ crystals. SR scattering should show an incidence angle dependence and a polarization dependence which would experimentally demonstrate the existence of an analogous black-hole in the type-III Dirac semi-metal $Ni_3In_2Se_2$.

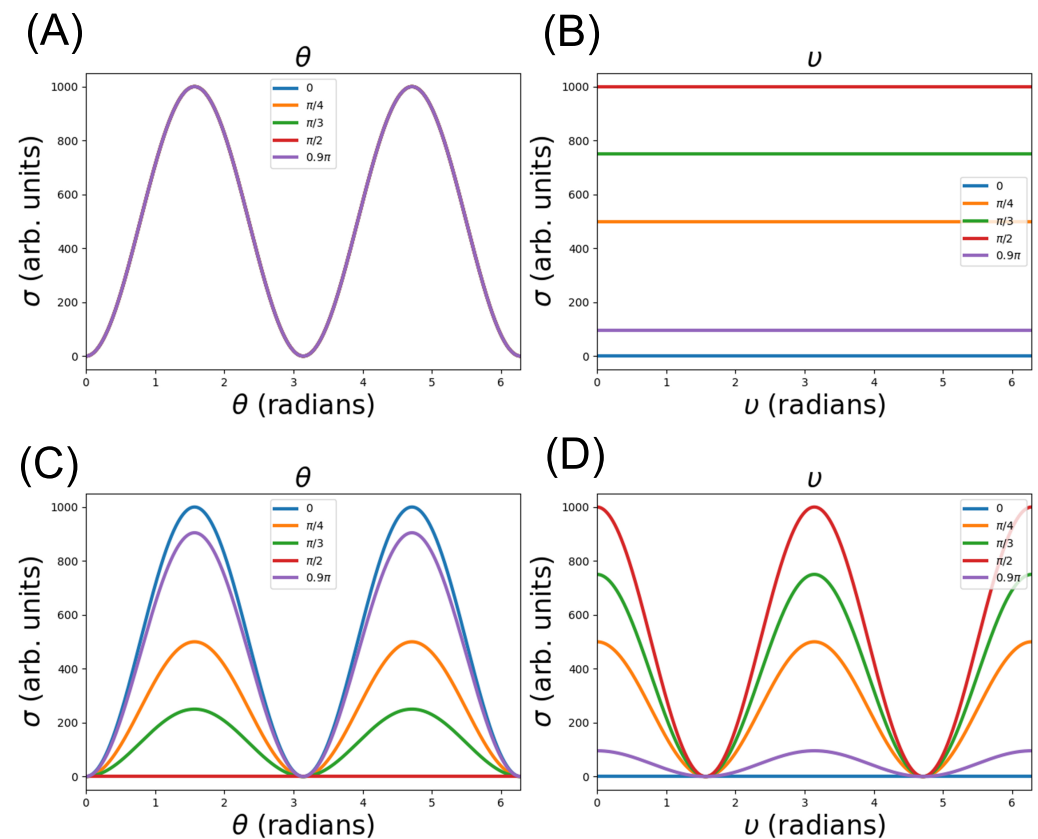**Figure 3.** Optical response: The optical response for a material that has a isotropic band structure (**A**) θ dependence, (**B**) υ dependence. The optical response of the strongly anisotropic type-III Dirac material with polarization angle (**A**) θ and (**B**) υ dependence. Highly Anisotropic response with (**C**) θ and (**D**) υ dependence. Angle dependence is set to $0, \pi/4, \pi/3, \pi/2, 0.9\pi$.

5. Conclusions

In conclusion, it is found that the SYK model with modifications, can capture the interaction of both a black hole with Majorana Fermions and Dirac Fermions. Upon studying the critically tilted Dirac cone, it can be seen that the Dirac Fermions behave in a similar manner to the Majorana Fermions in the SYK Black hole model. By utilizing this correlation it is possible to study black hole physics in condensed matter systems, opening up the possibility of studying quantum information paradoxes in a table top setting. Single crystals of $Ni_3In_2S_2$ and $Ni_3In_2Se_2$ have been shown theoretically to have perfectly flat and ideal type-III Dirac cones. Finally, an experiment is proposed to both confirm analogous black holes in type-III Dirac semimetals and to confirm the existence on super-radiant scattering.

Abbreviations

The following abbreviations are used in this manuscript:

SYK	Sachdev-Ye-Kitaev
SR	Super radiant

References

1. Hawking, S.W. Black hole explosions? *Nature* **1974**, *248*, 30–31. [CrossRef]
2. Bekenstein, J.D. Black Holes and Entropy. *Phys. Rev. D* **1973**, *7*, 2333–2346. [CrossRef]
3. Barceló, C.; Liberati, S.; Visser, M. Analogue Gravity. *Living Rev. Relativ.* **2005**, *8*, 12. [CrossRef]
4. Unruh, W.G. Experimental Black-Hole Evaporation? *Phys. Rev. Lett.* **1981**, *46*, 1351–1353. [CrossRef]
5. Knott, P.A.; Tufarelli, T.; Piani, M.; Adesso, G. Generic Emergence of Objectivity of Observables in Infinite Dimensions. *Phys. Rev. Lett.* **2018**, *121*, 160401. [CrossRef]
6. Cardoso, V.; Franzin, E.; Pani, P. Is the Gravitational-Wave Ringdown a Probe of the Event Horizon? *Phys. Rev. Lett.* **2016**, *116*, 171101. [CrossRef] [PubMed]
7. Steinhauer, J. Observation of quantum Hawking radiation and its entanglement in an analogue black hole. *Nat. Phys.* **2016**, *12*, 959–965. [CrossRef]
8. Belgiorno, F.; Cacciatori, S.L.; Clerici, M.; Gorini, V.; Ortenzi, G.; Rizzi, L.; Rubino, E.; Sala, V.G.; Faccio, D. Hawking Radiation from Ultrashort Laser Pulse Filaments. *Phys. Rev. Lett.* **2010**, *105*, 203901. [CrossRef] [PubMed]
9. Nikitin, I. Quantum Gravity Wormholes and Topological Teleporter. *arXiv* **2019**, arXiv:1909.08984.
10. Krishna, A.; Poulin, D. Topological wormholes: Nonlocal defects on the toric code. *Phys. Rev. Res.* **2020**, *2*, 023116. [CrossRef]
11. Jacobson, T.A.; Volovik, G.E. Effective spacetime and Hawking radiation from a moving domain wall in a thin film of 3He-A. *J. Exp. Theor. Phys. Lett.* **1998**, *68*, 874–880. [CrossRef]
12. Jacobson, T.; Koike, T. Black hole and baby universe in a thin film of 3He-A. In *Artificial Black Holes*; World Scientific: Singapore, 2002; pp. 87–108. [CrossRef]
13. Jacobson, T.A.; Volovik, G.E. Event horizons and ergoregions in3He. *Phys. Rev. D* **1998**, *58*, 064021. [CrossRef]
14. Volovik, G.E. Simulation of a Panlevé-Gullstrand black hole in a thin 3He-A film. *J. Exp. Theor. Phys. Lett.* **1999**, *69*, 705–713. [CrossRef]
15. Huhtala, P.; Volovik, G.E. Fermionic microstates within the Painlevé-Gullstrand black hole. *J. Exp. Theor. Phys.* **2002**, *94*, 853–861. [CrossRef]
16. Nissinen, J. Emergent Spacetime and Gravitational Nieh-Yan Anomaly in Chiral Weyl Superfluids and Superconductors. *Phys. Rev. Lett.* **2020**, *124*. [CrossRef] [PubMed]
17. Nissinen, J.; Volovik, G.E. Type-III and IV interacting Weyl points. *JETP Lett.* **2017**, *105*, 447–452. [CrossRef]
18. Dai, D.C.; Stojkovic, D. Observing a wormhole. *Phys. Rev. D* **2019**, *100*, 083513. [CrossRef]
19. Simonetti, J.H.; Kavic, M.J.; Minic, D.; Stojkovic, D.; Dai, D.C. A sensitive search for wormholes. *arXiv* **2020**, arXiv:2007.12184.
20. Sims, C. Topologically Protected Wormholes in Type-III Weyl Semimetal Co3In2X2 (X = S, Se). *Condens. Matter* **2021**, *6*, 18. [CrossRef]
21. Hasan, M.Z.; Kane, C.L. Colloquium: Topological insulators. *Rev. Mod. Phys.* **2010**, *82*, 3045. [CrossRef]
22. Qi, X.L.; Zhang, S.C. Topological insulators and superconductors. *Rev. Mod. Phys.* **2011**, *83*, 1057. [CrossRef]
23. Xu, S.Y.; Belopolski, I.; Alidoust, N.; Neupane, M.; Bian, G.; Zhang, C.; Sankar, R.; Chang, G.; Yuan, Z.; Lee, C.C.; et al. Discovery of a Weyl fermion semimetal and topological Fermi arcs. *Science* **2015**, *349*, 613–617. [CrossRef]
24. Lv, B.Q.; Weng, H.M.; Fu, B.B.; Wang, X.P.; Miao, H.; Ma, J.; Richard, P.; Huang, X.C.; Zhao, L.X.; Chen, G.F.; et al. Experimental Discovery of Weyl Semimetal TaAs. *Phys. Rev. X* **2015**, *5*, 031013. [CrossRef]

25. Huang, S.M.; Xu, S.Y.; Belopolski, I.; Lee, C.C.; Chang, G.; Wang, B.; Alidoust, N.; Bian, G.; Neupane, M.; Zhang, C.; et al. A Weyl Fermion semimetal with surface Fermi arcs in the transition metal monopnictide TaAs class. *Nat. Commun.* **2015**, *6*, 7373. [CrossRef]

26. Weng, H.; Fang, C.; Fang, Z.; Bernevig, B.A.; Dai, X. Weyl Semimetal Phase in Noncentrosymmetric Transition-Metal Monophosphides. *Phys. Rev. X* **2015**, *5*, 011029. [CrossRef]

27. Wan, X.; Turner, A.M.; Vishwanath, A.; Savrasov, S.Y. Topological semimetal and Fermi-arc surface states in the electronic structure of pyrochlore iridates. *Phys. Rev. B* **2011**, *83*, 205101. [CrossRef]

28. Borisenko, S.; Gibson, Q.; Evtushinsky, D.; Zabolotnyy, V.; Büchner, B.; Cava, R.J. Experimental Realization of a Three-Dimensional Dirac Semimetal. *Phys. Rev. Lett.* **2014**, *113*, 027603. [CrossRef] [PubMed]

29. Neupane, M.; Xu, S.Y.; Sankar, R.; Alidoust, N.; Bian, G.; Liu, C.; Belopolski, I.; Chang, T.R.; Jeng, H.T.; Lin, H.; et al. Observation of a three-dimensional topological Dirac semimetal phase in high-mobility Cd3As2. *Nat. Commun.* **2014**, *5*, 3786. [CrossRef]

30. Neupane, M.; Hosen, M.M.; Belopolski, I.; Wakeham, N.; Dimitri, K.; Dhakal, N.; Zhu, J.X.; Hasan, M.Z.; Bauer, E.D.; Ronning, F. Observation of Dirac-like semi-metallic phase in NdSb. *J. Phys. Condens. Matter* **2016**, *28*, 23LT02. [CrossRef]

31. Wang, Z.; Weng, H.; Wu, Q.; Dai, X.; Fang, Z. Three-dimensional Dirac semimetal and quantum transport in Cd3As2. *Phys. Rev. B* **2013**, *88*, 125427. [CrossRef]

32. Wang, Z.; Sun, Y.; Chen, X.Q.; Franchini, C.; Xu, G.; Weng, H.; Dai, X.; Fang, Z. Dirac semimetal and topological phase transitions inA3Bi (A = Na, K, Rb). *Phys. Rev. B* **2012**, *85*, 195320. [CrossRef]

33. Yan, M.; Huang, H.; Zhang, K.; Wang, E.; Yao, W.; Deng, K.; Wan, G.; Zhang, H.; Arita, M.; Yang, H.; et al. Lorentz-violating type-II Dirac fermions in transition metal dichalcogenide PtTe2. *Nat. Commun.* **2017**, *8*, 257. [CrossRef]

34. Huang, H.; Zhou, S.; Duan, W. Type-II Dirac fermions in the PtSe$_2$ Class of transition metal dichalcogenides. *Phys. Rev. B* **2016**, *94*, 121117. [CrossRef]

35. Hsieh, T.H.; Lin, H.; Liu, J.; Duan, W.; Bansil, A.; Fu, L. Topological crystalline insulators in the SnTe material class. *Nat. Commun.* **2012**, *3*, 982. [CrossRef]

36. Fang, C.; Weng, H.; Dai, X.; Fang, Z. Topological nodal line semimetals. *Chin. Phys. B* **2016**, *25*, 117106. [CrossRef]

37. Fu, L. Topological Crystalline Insulators. *Phys. Rev. Lett.* **2011**, *106*, 106802. [CrossRef] [PubMed]

38. Zhang, X.; Jin, L.; Dai, X.; Liu, G. Topological Type-II Nodal Line Semimetal and Dirac Semimetal State in Stable Kagome Compound Mg$_3$Bi$_2$. *J. Phys. Chem. Lett.* **2017**, *8*, 4814–4819. [CrossRef]

39. Zhang, X.; Yu, Z.M.; Sheng, X.L.; Yang, H.Y.; Yang, S.A. Coexistence of four-band nodal rings and triply degenerate nodal points in centrosymmetric metal diborides. *Phys. Rev. B* **2017**, *95*, 235116. [CrossRef]

40. Rosenhaus, V. An introduction to the SYK model. *J. Phys. A Math. Theor.* **2019**, *52*, 323001. [CrossRef]

41. Fragkos, S.; Tsipas, P.; Xenogiannopoulou, E.; Panayiotatos, Y.; Dimoulas, A. Type-III Dirac fermions in HfxZr1-xTe topological semimetal candidate. *J. Appl. Phys.* **2021**, *129*, 075104. [CrossRef]

42. Milićević, M.; Montambaux, G.; Ozawa, T.; Jamadi, O.; Real, B.; Sagnes, I.; Lemaître, A.; Gratiet, L.L.; Harouri, A.; Bloch, J.; et al. Type-III and Tilted Dirac Cones Emerging from Flat Bands in Photonic Orbital Graphene. *Phys. Rev. X* **2019**, *9*, 031010. [CrossRef]

43. Mizoguchi, T.; Matsuura, H.; Ogata, M. Thermoelectric transport of type-I, II, and III massless Dirac fermions in a two-dimensional lattice model. *Phys. Rev. B* **2022**, *105*, 205203. [CrossRef]

44. Volovik, G.E.; Zhang, K. Lifshitz Transitions, Type-II Dirac and Weyl Fermions, Event Horizon and All That. *J. Low Temp. Phys.* **2017**, *189*, 276–299. [CrossRef]

45. Zhang, T.; Yilmaz, T.; Vescovo, E.; Li, H.X.; Moore, R.G.; Lee, H.N.; Miao, H.; Murakami, S.; McGuire, M.A. Endless Dirac nodal lines in kagome-metal Ni3In2S2. *Npj Comput. Mater.* **2022**, *8*, 155. [CrossRef]

46. Giannozzi, P.; Baroni, S.; Bonini, N.; Calandra, M.; Car, R.; Cavazzoni, C.; Ceresoli, D.; Chiarotti, G.L.; Cococcioni, M.; Dabo, I.; et al. QUANTUM ESPRESSO: A modular and open-source software project for quantum simulations of materials. *J. Phys. Condens. Matter* **2009**, *21*, 395502. [CrossRef]

47. Perdew, J.P.; Burke, K.; Ernzerhof, M. Generalized Gradient Approximation Made Simple. *Phys. Rev. Lett.* **1996**, *77*, 3865–3868. [CrossRef]

48. Corso, A.D. Pseudopotentials periodic table: From H to Pu. *Comput. Mater. Sci.* **2014**, *95*, 337–350. [CrossRef]

49. Jain, A.; Ong, S.P.; Hautier, G.; Chen, W.; Richards, W.D.; Dacek, S.; Cholia, S.; Gunter, D.; Skinner, D.; Ceder, G.; et al. Commentary: The Materials Project: A materials genome approach to accelerating materials innovation. *APL Mater.* **2013**, *1*, 011002. [CrossRef]

50. Sims, C.; Hosen, M.M.; Aramberri, H.; Huang, C.Y.; Dhakal, G.; Dimitri, K.; Kabir, F.; Regmi, S.; Zhou, X.; Chang, T.R.; et al. Termination-dependent topological surface states in nodal-loop semimetal HfP2. *Phys. Rev. Mater.* **2020**, *4*, 054201. [CrossRef]

51. Hinuma, Y.; Pizzi, G.; Kumagai, Y.; Oba, F.; Tanaka, I. Band structure diagram paths based on crystallography. *Comput. Mater. Sci.* **2017**, *128*, 140–184. [CrossRef]

52. Togo, A.; Tanaka, I. Spglib: A software library for crystal symmetry search. *arXiv* **2018**, arXiv:1808.01590.

53. Fisk, Z.; Remeika, J.P. Chapter 81 Growth of single crystals from molten metal fluxes. *Handb. Phys. Chem. Rare Earths* **1989**, *12*, 53–70. [CrossRef]

54. Canfield, P.C.; Fisk, Z. Growth of single crystals from metallic fluxes. *Philos. Mag. B* **1992**, *65*, 1117–1123. [CrossRef]

55. Sachdev, S.; Ye, J. Gapless spin-fluid ground state in a random quantum Heisenberg magnet. *Phys. Rev. Lett.* **1993**, *70*, 3339–3342. [CrossRef]

56. Polchinski, J.; Rosenhaus, V. The spectrum in the Sachdev-Ye-Kitaev model. *J. High Energy Phys.* **2016**, *2016*, 1–25. [CrossRef]

57. Maldacena, J.; Stanford, D. Remarks on the Sachdev-Ye-Kitaev model. *Phys. Rev. D* **2016**, *94*, 106002. [CrossRef]
58. Bernard, D.; LeClair, A. A classification of 2D random Dirac fermions. *J. Phys. A Math. Gen.* **2002**, *35*, 2555–2567. [CrossRef]
59. Seo, J.W.; Yuk, T.; Han, Y.K.; Sin, S.J. ABC-stacked multilayer graphene in holography. *J. High Energy Phys.* **2022**, *2022*, 17. [CrossRef]
60. Landsteiner, K.; Liu, Y.; Sun, Y.W. Quantum Phase Transition between a Topological and a Trivial Semimetal from Holography. *Phys. Rev. Lett.* **2016**, *116*, 081602. [CrossRef]
61. Gao, L.L.; Liu, Y.; Lyu, H.D. Black hole interiors in holographic topological semimetals. *J. High Energy Phys.* **2023**, *2023*, 34. [CrossRef]
62. Fan, R.; Sun, L.; Shao, X.; Li, Y.; Zhao, M. Two-dimensional Dirac materials: Tight-binding lattice models and material candidates. *ChemPhysMater* **2023**, *2*, 30–42. [CrossRef]
63. Lim, J.; Ooi, K.J.A.; Zhang, C.; Ang, L.K.; Ang, Y.S. Broadband strong optical dichroism in topological Dirac semimetals with Fermi velocity anisotropy. *Chin. Phys. B* **2020**, *29*, 077802. [CrossRef]
64. Saberi-Pouya, S.; Vazifehshenas, T.; Salavati-fard, T.; Farmanbar, M.; Peeters, F.M. Strong anisotropic optical conductivity in two-dimensional puckered structures: The role of the Rashba effect. *Phys. Rev. B* **2017**, *96*, 075411. [CrossRef]
65. Bini, D.; Cherubini, C.; Jantzen, R.T.; Ruffini, R. Teukolsky Master Equation: De Rham Wave Equation for Gravitational and Electromagnetic Fields in Vacuum. *Prog. Theor. Phys.* **2002**, *107*, 967–992. [CrossRef]
66. Yagi, K.; Stein, L.C. Black hole based tests of general relativity. *Class. Quantum Gravit.* **2016**, *33*, 054001. [CrossRef]
67. Dolan, S.R.; Dempsey, D. Bound states of the Dirac equation on Kerr spacetime. *Class. Quantum Gravit.* **2015**, *32*, 184001. [CrossRef]
68. Brito, R.; Cardoso, V.; Pani, P. Black holes as particle detectors: Evolution of superradiant instabilities. *Class. Quantum Gravit.* **2015**, *32*, 134001. [CrossRef]
69. Herdeiro, C.; Radu, E. Construction and physical properties of Kerr black holes with scalar hair. *Class. Quantum Gravit.* **2015**, *32*, 144001. [CrossRef]
70. Prain, A.; Maitland, C.; Faccio, D.; Marino, F. Superradiant scattering in fluids of light. *Phys. Rev. D* **2019**, *100*, 024037. [CrossRef]